JAAS

ROYAL SOCIETY OF CHEMISTRY

PAPER

View Article Online
View Journal | View Issue

Cite this: *J. Anal. At. Spectrom.*, 2025, **40**, 2447

Operando laboratory XAS on battery materials using the DANOISE cell in a von Hámos spectrometer

Sebastian Praetz, †*[a] Morten Johansen, †‡[b] Delf Kober,[c] Marko Tesic,[a] Christopher Schlesiger,[a] Dorthe Bomholdt Ravnsbæk[b] and Birgit Kanngießer[a]

This work presents laboratory-based *operando* X-ray absorption spectroscopy (XAS) measurements on electrodes for rechargeable batteries. Using the "Developed in Aarhus: New *Operando* In-house Scattering Electrochemical" (DANOISE) cell, *operando* XAS measurements were performed with two von Hámos spectrometers, optimized for X-ray absorption near edge structure (XANES) and extended X-ray absorption fine structure (EXAFS). Selected battery electrodes, including commercial $LiFePO_4$ (LFP) for Li-ion batteries and layered transition metal oxides, Na_xTMO_2 (TM = Fe, Mn), electrodes for Na-ion batteries, were measured to present a proof of principal for the applicability of these spectrometers in battery research. The von Hámos spectrometers used in this study offer a high efficiency and the ability to measure a large spectral bandwidth (up to 1500 eV beyond the edge). Fe K-edge XANES measurements of LFP with an acquisition time of 15 minutes per spectrum successfully captured the transition of Fe species to $FePO_4$ during cycling. Additionally, Mn K-edge XANES measurements on Na-ion battery materials highlight the challenges associated with Na-ion batteries, particularly due to their higher absorption compared to Li-ion counterparts. Nevertheless, the Mn K-edge was successfully measured, allowing for oxidation state determination in the material. Fe K-edge EXAFS measurements on Na-ion battery materials revealed the transition of Fe species during charging, within an acquisition time of 15 to 25 minutes.

Received 22nd April 2025
Accepted 22nd July 2025

DOI: 10.1039/d5ja00155b

rsc.li/jaas

1 Introduction

Rechargeable batteries are crucial in moving modern society towards a more sustainable future powered by renewable and green energy sources. Between 2020 and 2023, the International Energy Agency (IEA) reported a fourfold increase in the global energy-storage capacity using Li-ion batteries.[1] This development creates a constant push for new and improved rechargeable battery technologies.[2] A key aspect is to lower the cost and improve the sustainability of the functional battery materials as the most widely employed battery technologies primarily rely on scarce or critical minerals such as lithium and cobalt.[3] This is a challenge as battery performance is closely linked to the chemical composition of the functional materials. Simultaneously, novel battery technologies must be competitive and preferably surpass current rechargeable battery performance.[2,4]

Optimizing, designing and developing new technologies require a profound understanding of the functional materials hereunder, the active electrode materials, which should preferably be studied during charge and discharge, as the dynamic conditions in an operating battery are far from equilibrium. X-rays are extensively used to probe the changes in an operating battery using various *operando* diffraction or absorption techniques.[5] Powder X-ray diffraction (PXRD) reveals the changes in the crystal structure of the active battery materials, while element-specific changes in valence state and the local atomic environment can be probed using XAS.[6] Having the two as complementary techniques makes a strong analytical tool, allowing for, *e.g.* coupling structural transitions directly to the redox activity of a specific element.

XAS, also referred to as X-ray absorption fine structure (XAFS) spectroscopy, is typically divided into two regions: XANES and EXAFS. This well-established and highly versatile method is widely used to study the electronic structure of atoms, as well as the coordination and bonding distances between them. Due to the high brilliance and flux achievable in synchrotron radiation facilities, *operando* experiments are often carried out at these

[a]*Technische Universität Berlin, Institute of Physics and Astronomy, Sekr. EW 3-1, Hardenbergstraße 36, 10623 Berlin, Germany. E-mail: sebastian.praetz@tu-berlin.de*
[b]*Aarhus University, Department of Chemistry, Center for integrated Materials Research, Langelandsgade 140, DK-8000 Aarhus, Denmark*
[c]*Technische Universität Berlin, Faculty III Process Sciences, Institute of Materials Science and Technology, Chair of Advanced Ceramic Materials, Straße des 17 Juni 135, 10623 Berlin, Germany*
† These authors contributed equally to this work.
‡ Present address: Deutsches Elektronen-Synchrotron (DESY), Notkestrasse 85, 22607 Hamburg, Germany.

large-scale facilities.[7–9] However, it is worth noting that *operando* XAS has been applied in battery research for more than two decades. Pioneering contributions by McBreen,[10] Cramer,[11] Wagemaker,[12] and others laid the groundwork for many of today's in-depth mechanistic studies. XAS has also gained traction in laboratory environments with the advent of advanced laboratory spectrometers.[13–18] The laboratory spectrometers used in this work already demonstrated their capabilities to measure *ex situ* within the fields of catalysis research,[19–25] material science[26–29] and other.[30,31] As shown by recent works of Kallio *et al.* and Praetz *et al.*, among other, laboratory XAS spectrometer are not limited to *ex situ* measurement.[32–35] Using laboratory-based X-ray sources for *operando* studies creates flexibility and options for material screening, which is a great aid for scientific progress and promotes the development of novel battery technologies. While the high brilliance and flux of synchrotron radiation sources offers a high versatility, *e.g.*, to probe low concentrations or reach a high temporal resolving power, especially for time consuming studies such as long-term degradation of batteries or routine analysis, laboratory-based methods have an advantage over synchrotron-based techniques, where access and beam time are limited. Additionally, laboratory measurements can also complement synchrotron experiments to efficiently render beam time or accelerate material development when rapid feedback is required.

Operando XAS battery studies naturally require a suitable battery cell that is easy to assemble, transparent to X-rays at the desired photon energies, provides a high and homogeneous stack pressure, ensures good electronic contact to the stack and an airtight battery cavity to prevent air poisoning of the battery components.[36] These are all features that the DANOISE cell[34] fulfills (see Fig. 1). The two 300 μm thin glassy carbon (SIGRADUR® G, Hochtemperatur Werkstoffe GmbH) windows, ensure 49%[37] transmission at the Mn K-edge (6.538 keV[38]) and 58%[37] at the Fe K-edge (at 7.112 keV[38]). The high rigidness and precise manufacturing of glassy carbon windows ensure a homogeneous and high stack pressure. The large pinhole diameter (∅ 10 mm) of the cell accommodates the larger beam size of laboratory spectrometers, enabling a more efficient use of the incoming photons. In addition to its use as an *operando* cell, it can also serve as an inert environment for sensitive sample systems.

In this work, investigations on different battery materials were conducted by measuring the absorption K-edge of two different 3d-elements (Fe and Mn) to provide a proof of principle for the applied von Hámos spectrometers. The main focus of the manuscript is to demonstrate and discuss the capabilities and limitations of the spectrometer for *operando* battery research. In addition to the investigation of the Fe K-edge in LFP, which is widely used as a cathode material in batteries due to its low cost and long cycle life,[39] Na-ion batteries were analyzed at the Mn and Fe K-edges. Na-ion batteries are becoming increasingly important alternatives due to their higher abundance, lower production costs, and reduced environmental impact compared to Li-ion batteries.[40]

2 Experimental section

In Section 2.1 the cell design (Section 2.1.1), the synthesis of Na-ion battery cathodes (Section 2.1.2) and the electrode preparation and assembly of the cell (Section 2.1.3) will be described. Furthermore, the electrochemical cycling of the cell is explained in Section 2.1.4. In Section 2.2 the used laboratory XAS setups are discussed. Finally, reference materials, along with the synthesis procedure for the LFP standard, are presented in Section 2.3.

2.1 DANOISE cell

2.1.1 Cell design. The concept of the DANOISE (Developed in Aarhus: New *Operando* In-house Scattering Electrochemical) cell[34] is inspired by the AMPIX cell (Borkiewicz *et al.*, 2012)[41] and is compatible with multiple X-ray scattering and spectroscopy methods, including X-ray diffraction (XRD), small-angle X-ray scattering (SAXS) and XAS.[34] The cell and its components are shown in Fig. 1 (left). The cell consists of a bottom and top part 3D printed with a polylactic acid (PLA) filament,[42] a ∅ 10 mm pinhole covered by a ∅ 20 mm glassy carbon window (300 μm SIGRADURA® G, HTW Hochtemperatur Werkstoffe GmbH)[43] fastened using conductive silver epoxy. Electrical contact for the cell is facilitated through these glassy carbon windows, which are connected to external 2 mm banana jacks.

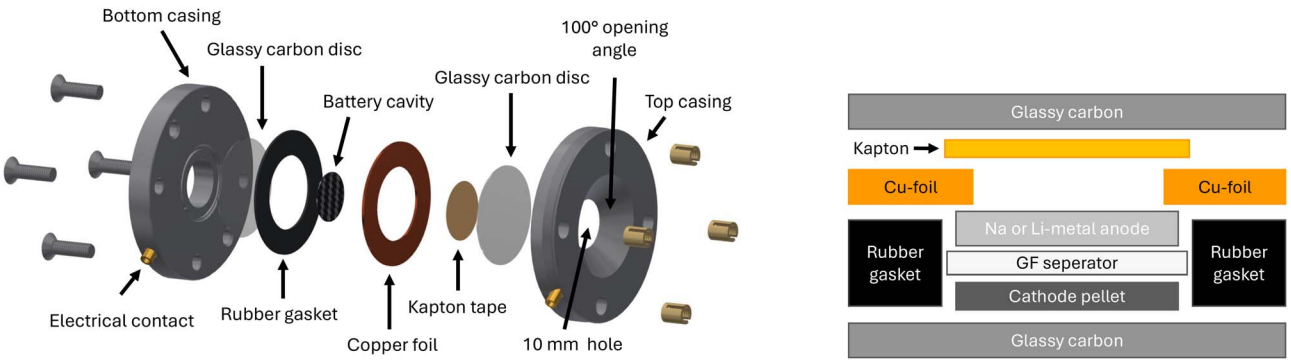

Fig. 1 (Left) Exploded view of the DANOISE cell. (Right) Schematic view through the battery cavity of the DANOISE cell with the battery stack composed of anode, GF/B separator and cathode pellet. The illustration is based on Johansen *et al.* 2024.[34]

The top part has an additional opening angle of 100° for *e.g.* XRD. Inside the cell, a 0.8 mm thick fluorosilicone rubber gasket prevents direct physical contact between the glassy carbon windows, thereby avoiding a short circuit between the two poles, and seals the battery cavity to protect the stack from air exposure. The battery stack comprises the anode material (Li or Na-metal), a Whatman glass fiber (GF/B) separator, and a free-standing cathode pellet. Hence, the stack is a two-electrode cell, wherein the metal anode served both as the reference and counter electrode. A thin disc of Kapton® tape placed on the anode window prevents the intercalation of Li or Na into the glassy carbon structure. Due to the insulating nature of Kapton®, a Cu-foil ring is placed between the Kapton®-covered window and the anode side of the battery cavity. Fig. 1 (right) shows a schematic view through the assembled cell. For more details, we refer to Borkiewicz *et al.* 2012 [41] and Johansen *et al.* 2024.[34]

2.1.2 Synthesis of layered Na-ion battery cathodes. Layered O3-type materials $Na_{0.72}Fe_{0.6}Mn_{0.4}O_2$ (denoted F6M4), $Na_{0.84}Fe_{0.6}Mn_{0.3}Mg_{0.1}O_2$ (denoted FMM) and $Na_{0.78}Fe_{0.45}Mn_{0.45}Ti_{0.1}O_2$ (denoted FMT) were synthesized using Mn_2O_3 (>99.9%, Sigma Aldrich), Fe_2O_3 (99.8%, Alfa Aesar), anhydrous Na_2CO_3 (99.8%, VWR Chemicals) and anatase-TiO_2 or MgO (99.8%, Sigma Aldrich) for the dopant. The different precursors were weighed according to Table 1 and transferred to an 80 mL tungsten carbide (WC) crucible for high-energy ball milling containing 10 WC ∅ 10 mm balls (7.8 g per ball) giving a ball-to-powder mass ratio of 40 : 1. After adding ∼1 mL acetone, the crucibles were closed, and the mixtures were milled using a Pulverisette P6 for 30 min at 400 rpm using ten repetitions of 3 minutes milling and 4 minutes resting. The precursor mixture was subsequently pressed into a ∅ 20 mm pellet under an uniaxial pressure of 3 tonnes for one minute. The pellet was heated to 900 °C at 300 °C h^{-1} rate, annealed for 16 h, cooled down, and transferred to an Ar-filled glove box before cooling below 300 °C.

2.1.3 Electrode preparation and cell assembly. Free-standing cathode pellets of LFP (MTI Corporation) and FMT were prepared by mixing the active material with polyvinylidene fluoride binder (HSV900, MIT), acetylene black (VXC72, Cabot Corporation) and graphite (C-NERGY SFG6L, IMERYS) in a mass ratio of 4 : 2 : 2 : 2. Cathode pellets of F6M4 and FMM were prepared by mixing active cathode material, polyvinylidene binder (HSV900, MIT) and carbon black (C-NERGY Super C45, IMERYS) in a 44 : 33 : 23 mass ratio. This results in Fe concentrations ranging from 13 wt% to 14 wt% for LFP, F6M4, and FMM pellets, and 9 wt% Mn for the FMT pellet. The mixed powders were transferred to an agate mortar, and the components were carefully mixed under an inert Ar-atmosphere to obtain a homogeneous composite. The free-standing pellets were obtained by applying an uniaxial pressure of 2 tonnes for one minute. To accommodate the relatively large X-ray beam size, pellets of ∅ 8.5 mm and ∅ 10 mm were used for the LFP and Na-ion battery materials, respectively. All pellets were prepared to obtain an absorption length between 2 and 3 for 50 eV (7162 eV) above the Fe K-edge[38] using the XAFSmass[44] program.

Operando laboratory XAS was performed using the DANOISE[34] cell mounted at the spectrometer (see Section 2.2) directly in front of the X-ray source, at a distance of approximately 8 cm from the source spot. LFP was cycled against a 50 μm thick Li-metal disc serving as the anode with a Whatman GF/B separator wetted with eight drops of 1 M solution of lithium hexafluorophosphate ($LiPF_6$) in a 1 : 1 v/v mixture of ethylene carbonate and dimethyl carbonate (99.9%, Solvionic). The Na-ion battery cathodes were cycled against a thinly rolled Na-metal disc separated from the cathode pellet by a Whatman GF/B separator wetted with eight drops of a 1 M solution of sodium trifluoromethanesulfonimide (NaTFSI) in a 1 : 1 v/v mixture of ethylene carbonate and dimethyl carbonate (99.9%, Solvionic) serving as the electrolyte. Lithium-containing cells were assembled in an Ar-filled glovebox while Na-containing cells were assembled under N_2-atmosphere.

2.1.4 Electrochemical cycling. The batteries were cycled at a current rate of C/10 within potential limits of 2.5–4.2 V *vs.* Li^+/Li for LFP and at a current rates of C/20 for F6M4 and C/15 for FMM and FMT within the potential limits of 1.5–4.3 V Na^+/Na. The electrochemical cycling was controlled using a Yokogawa GS610 potentiostat and a self-written LabVIEW program. After charging and discharging, pausing steps of up to 2 hours for relaxation were conducted. The theoretical gravimetric capacity, which will be compared to the measured capacity in the following (see Section 3), is calculated based on the complete extraction of one Li (or Na for F6M4, FMM and FMT) ion per formula unit from the cathode.

Table 1 The masses of different precursors used for synthesizing $Na_{0.72}Fe_{0.6}Mn_{0.4}O_2$ (F6M4), $Na_{0.84}Fe_{0.6}Mn_{0.3}Mg_{0.1}O_2$ (FMM) and $Na_{0.78}Fe_{0.45}Mn_{0.45}Ti_{0.1}O_2$ (FMT). See PXRD Rietveld refinement profiles and structural information for the as-synthesized materials in Section 2.1 of the SI

	Precursor			
Sample	Mn_2O_3/g	Fe_2O_3/g	Na_2CO_3/g	Dopant/g
F6M4	0.4283	0.6508	0.7193	
FMM	0.4283	0.6508	0.7193	0.0560
FMT	0.5399	0.5464	0.7405	0.1214

2.2 Laboratory XAS setups

XAS measurements were carried out with two self-developed wavelength-dispersive spectrometers in von Hámos geometry – one optimized for EXAFS measurements, and the other for XANES measurements with short acquisition times.[16,45] The spectrometers are equipped with a micro focus X-ray tube, a curved Highly Annealed Pyrolytic Graphite (HAPG) mosaic crystal and a hybrid photon counting CMOS detector with 512 × 1030 pixel and a pixel size of 75 × 75 μm. The X-ray tube is optimized to reach 30 W at 15 kV with an emission angle of 18° and a source spot of 70 × 70 μm. For the Fe K-edge measurement the tube was operated with a voltage of 13.5 kV and a current of 1790 μA and for the Mn K-edge measurement with a voltage of 12.2 kV and current of 1580 μA. The sample or cell is positioned directly in front of the X-ray source, at a distance of

approximately 8 cm from the source spot. The distances to the optic and the detector depend on the selected X-ray energy and the type of optic used, and increase with higher energy and a larger bending radius of the optic. Due to the von Hamos geometry, the area illuminated by the divergent X-ray beam is larger than the sample area effectively detected by the spectrometer. The simultaneously measured sample area depends on the set energy and typically covers a few square millimeters. These von Hámos spectrometers are measuring the whole spectral bandwidth simultaneously, which means scan free without any moving parts during the measurements. The differences between the two spectrometers, primarily arising from the use of different HAPG optics, are discussed in more detail in the following sections.

2.2.1 XANES. The XANES optimized spectrometer employs a dispersive optic with a crystal thickness of 40 μm, a bending radius of 150 mm, and a length of 5 cm in the dispersive plane. It is optimized for short time XANES acquisition with a spectral resolving power of at least $E/\Delta E \approx 2000$,[46] offering significantly shorter measurement times than optics optimized solely for highest resolution, such as demonstrated by Schlesiger *et al.* 2020.[45] In our setup, measurement times of approximately 5 minutes per spectrum are sufficient to quantify fractions of pure iron oxide mixtures *via* linear combination fitting (LCF), as shown in Schlesiger *et al.* 2015.[16]

In comparison, synchrotron-based XANES enables significantly faster data acquisition (<30 s) due to higher photon flux.[7] In *operando* experiments, the acquisition time directly influences the applicable C-rate, as each spectrum represents an average over the state-of-charge changes occurring during exposure. To ensure sufficient temporal resolution, the C-rate and acquisition time must be balanced such that the state-of-charge change per spectrum is limited to a few percent.

The spectral bandwidth which can be measured at the same time is about 500 eV. Vacuum tubes (5 mbar pressure inside) with 35 μm Kapton® windows are installed between the X-ray source and crystal and between the crystal and detector to lower the air absorption and increase the efficiency of the spectrometer.

2.2.2 EXAFS. The EXAFS optimized spectrometer uses a dispersive optic with a crystal thickness of 40 μm, a bending radius of 100 mm and a length of 16 cm in the dispersive plane. With this optic it is possible to measure a spectral bandwidth of 1500 eV at the Fe K-edge simultaneously. While the spectral bandwidth and the efficiency (better signal-to-noise ratio (SNR) in the same measurement time) is higher compared to the XANES optimized spectrometer, the resolving power of $E/\Delta E =$ 1500 to 1800 at the absorption edge,[45] but strongly decreasing with increasing energy, is lower. To reduce air absorption and increase efficiency, all components are in a vacuum chamber with an inside pressure of 5 mbar.

A side-by-side comparison of spectra measured with the EXAFS optimized and XANES optimized setup, highlighting the differences between the two spectrometers, is shown in the SI in Fig. S27–S29.

In the following, we refer to measurements performed using the XANES optimized optical setup as XANES optimized measurements, and to those conducted using the EXAFS optimized setup as EXAFS optimized measurements.

2.3 Reference materials

For the Fe K-edge measurements of the LFP two reference materials have been measured. For the discharged state of the LFP-cell, as-synthesized LFP was used. LFP was prepared by combination of two co-precipitation reactions and subsequent hydrothermal treatment after Chen *et al.* 2006 [47] and Lee *et al.* 2011.[48] As starting materials $LiOH \cdot H_2O$ (>98%, Merck), $FeSO_4 \cdot 7H_2O$ (>99%, p.a, Roth) and H_3PO_4 (85%, p.a, Chemsolute) were used. H_3PO_4 was dropwise added to $LiOH \cdot H_2O$ until pH of 8 and precipitation of Li_3PO_4 was observed. $FeSO_4 \cdot 7H_2O$ was dissolved in destilled water and dropwise added to the mixture until pH of 7 and precipitation of $Fe_3(PO_4)_2 \cdot 8H_2O$ was reached. The solution, including precipitate, was transferred directly into an autoclave and underwent a hydrothermal treatment at 120 °C for 5 hours to form $LiFePO_4$. The resulting LFP powder was filtered off and dried. In order to prevent the oxidation of Fe(II) to Fe(III) all steps were performed in Ar-atmosphere. Fig. S8 in the SI shows the XRD pattern of the synthesized LFP. All diffraction peaks can be indexed to an orthorhombic *Pnma* lattice structure, which is characteristic of $LiFePO_4$. The powder pattern was measured between 18° and 70° 2θ using a Bruker D8 Diffractometer (Bruker, Germany) with Co Kα radiation. Rietveld refinement on the XRD data was done with Diffrac TOPAS software.[49,50]

For the charged state of LFP, $FePO_4 \cdot 4H_2O$ (FP, ≥24% Fe, Sigma-Aldrich)[51] powder was purchased and used without further purification. The synthesized LFP and FP were prepared as pellets with 13 mm diameter by using a hydraulic pellet press and adding Hoechst Wax C as a binder. Different manganese oxides (MnO, MnO_2 and Mn_2O_3) were already prepared on adhesive tape and were used as references for the Mn K-edge investigation of the FMT cathode material. Furthermore, for the EXAFS measurements of F6M4 and FMM different iron oxides (FeO,[52] Fe_2O_3 [53] and Fe_3O_4 [54]), already prepared as powder on adhesive tape, were used as references.

3 Results

Section 3.1 presents the results measured with the XANES optimized setup on the commercial LFP and the synthesized FMT. This is followed by the results with the EXAFS optimized setup on F6M4 and FMM in Section 3.2. A demonstration of the capabilities and limitations of laboratory XANES and EXAFS optimized measurement for *operando* application is presented. The absorption is expressed in units of μQ (where μ is the mass attenuation coefficient and Q is the mass deposition of the analyte). The normalization and further processing of the data was done by using ATHENA of the Demeter software package.[55]

3.1 XANES on LFP and FMT

The *operando* XANES optimized measurement (see Section 2.2.1) for the commercial LFP material has been performed at the Fe K-edge and for the FMT material (see Section 2.1.2) at the Mn K-edge as a proof of concept for von Hámos *operando* XAS

measurement. The results of the *operando* XANES optimized measurements of charging LFP against a Li-metal anode with the corresponding galvanostatic potential profile are shown in Fig. 2. A spectrum was recorded every 300 s. To improve the data quality 3× binning of the data was applied resulting in 900 s (15 min) measurement time per spectrum. The complete charge process took about 9 h resulting in a total of 36 (3× binned) spectra in Fig. 2 (top). The full potential profile of the charge–discharge cycle, along with the unnormalized data, is provided in the SI in Fig. S1 and in Fig. S9 and S10 respectively. The change of the Fe K-edge as Li is extracted from LFP is clearly recognizable in the spectra shown in Fig. 2. This is also in agreement with the results presented in Johansen *et al.* 2024 [34] were *operando* XANES measurement has been performed on $LiFePO_4$ using the HelXAS spectrometer at the Center for X-ray Spectroscopy at the University of Helsinki.[18] The results for LFP in Fig. 2 (top) further indicate that upon completion of the charging period and reaching the potential limit of 4.2 V *vs.* Li^+/Li, the Fe in the cell is not fully converted to $FePO_4$. The theoretical specific capacity for LFP is 170 mA h g^{-1} (based on extraction of one Li), while the actual obtained capacity was 151 mA h g^{-1}, which explains this observation.

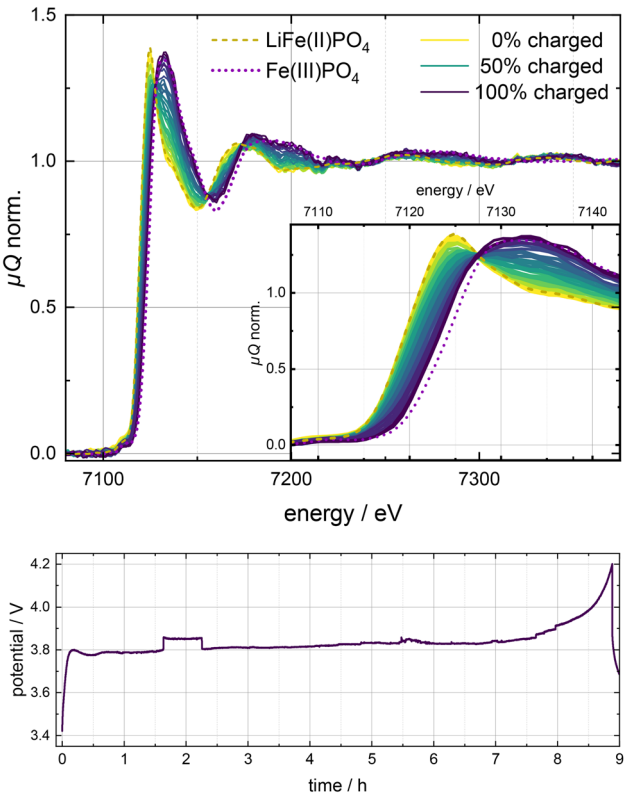

Fig. 2 (Top) Normalized XANES spectra recorded with the XANES optimized setup, during charge from 3.4 V to 4.2 V at a constant current of 115 μA, shown together with the references (dashed and dotted line) of $LiFePO_4$ and $FePO_4$. The 0% and 100% charged samples refers to the points at the lower and upper potential limits, while 50% is the time-point in the middle between the two. A capacity of 151 mA h g^{-1} was measured at the potential limit. (Bottom) The galvanostatic potential profile collected during charge of $LiFePO_4$ *vs.* Li^+/Li at C/10. The complete profile of charge and discharge is shown in the SI (see Fig. S1).

LCF of the first and last spectra of the charge cycle, performed over a broad energy window (24 eV below to 250 eV above the absorption edge), using $LiFePO_4$ and $FePO_4$ as reference standards, yields 100% ± 1% $LiFePO_4$ for the initial spectrum, while the final spectrum indicates 83% ± 1% $FePO_4$. These fits are shown in Fig. S11 (SI). To improve the quality of the fit in the region most sensitive to changes in oxidation state and local structure, an additional LCF analysis was performed in a narrower energy window (from 24 eV below to 30 eV above the absorption edge). This restricted range emphasizes the white line region (approximately 7125–7150 eV), which contains the most diagnostic information on speciation. This approach, illustrated in Fig. S12 (SI), minimizes the influence of multiple scattering at higher energies and allows a more focused evaluation of changes in the white line shape, in line with established XAS methodology.[56] While the narrow-window fitting more directly targets the white line feature, the overall trend in the weighted components remains consistent with the full-range fit, with no significant differences observed within the fit uncertainties. The evolution of the fitted component weights across all 36 spectra during charging is presented in Fig. S13 (SI).

Additionally, the Fe K-edge position was determined by interpolating the energy at μQ norm. = 0.5 of the normalized spectrum (Fig. S14, SI), showing a shift from the LFP reference toward—but not reaching—the $FePO_4$ reference. This supports the 83% $FePO_4$ fraction obtained by LCF at the end of charge. While we note that edge position alone is not a direct measure of oxidation state, its evolution agrees with the trends observed *via* LCF. Together with the persistence of isosbestic points at approximately 7127 eV, 7160 eV, and 7175 eV, this supports a two-phase equilibrium mechanism during charging,[57] which could be corroborated through principal component analysis (PCA) techniques,[58–60] however, such an analysis exceeds the scope of the present work.

The investigation of sodium (Na)-based batteries presents greater challenges compared to those of LFP as a result of the higher absorption by the metallic Na-anode. Furthermore, these cathode materials, compared to LFP used in this work, typically contain additional 3d transition metals (TM), such as Fe, Mn and Ti in the case of FMT, which further increases overall absorption. Additionally, the usable photon flux of the spectrometer decreases with lower photon energies, leading to a longer measurement time at the Mn K-edge (6539 eV) compared to the Fe K-edge (7112 eV) to achieve the same SNR for the same elemental concentration.[38]

Due to electrochemical malfunction of the battery cell containing the FMT electrode – potentially caused by improper stack pressure or an improper assembly – it was not possible to obtain a complete C/15 dataset. Charging the cell at a C/15 rate abruptly ended after 600 s when the potential limit of 4.3 V *vs.* Na^+/NA was reached. A discharge to reset/restart the battery cell resulted only in a charge period of approximately 1 h. The galvanostatic potential profile collected during this process is presented in the SI (see Fig. S2). Therefore, no adequate

operando XAFS measurement during charge and discharge could be conducted.

Nevertheless, despite these challenges, XANES spectra at the Mn K-edge of FMT within a battery stack in the DANOISE cell were successfully measured, allowing for the identification of the Mn oxidation state. Fig. 3 shows the normalized XANES spectra of FMT with three different binning intervals, corresponding to measurement times of 5 min, 15 min and 25 min, in comparison with reference spectra of Mn_2O_3 and MnO_2. The unnormalized data of the first 14 spectra with a 3× binning of the FMT during the charge and discharge attempts are provided in the SI in Fig. S15, which shows an overall absorption of the cell of $\mu Q > 7$ and an edge step/jump of about 0.7 μQ. When comparing the normalized FMT results in Fig. 3 with the reference spectra, the best description is obtained using MnO_2, suggesting that the Mn oxidation sate in FMT is mainly Mn(IV). For pristine FMT (prior to any electrochemical cycling), an oxidation state between Mn(III) and Mn(IV) is expected as the Na-content is usually ~5% below <1 in the as-synthesized material. LCF of the 5× binned FMT spectra prior to electrochemical cycling was performed using MnO, Mn_2O_3 and MnO_2 as reference standards (see SI Fig. S15, right). The LCF results indicate a composition of 30% ± 5% Mn_2O_3 and 70% ± 5% MnO_2, corresponding to an Mn(IV) oxidation state of approximately 70%. LCF on the 3× binned data results in the same composition for the oxidation state/species.

Despite the challenging absorption conditions of this sodium-based battery cell, the data quality of the Mn K-edge measurement is sufficient to qualitatively investigate the oxidation state of FMT within a 15 minutes measurement time frame.

3.2 EXAFS on F6M4 and FMM

The EXAFS optimized measurements (see Section 2.2.2) were performed at the Fe K-edge for the synthesized layered Na-ion battery F6M4 and FMM (see Section 2.1.2). In Fig. 4 (top, left) the normalized EXAFS spectra of F6M4 during the charge cycle is shown. The binning for this data set was 3×, resulting in 15 min measurement time per spectrum. The C/20 charge took about 12 h to reach the potential limit of 4.3 V *vs.* Na^+/Na (see Fig. S3 in the SI) resulting in 48 spectra. The unnormalized data is shown in Fig. S16 in the SI. Despite the higher total absorption of >5.5 μQ after the edge, compared to LFP, which is caused by the metallic Na-anode and the additional TM Mn in the cell, the data quality is comparable to the LFP measurement. Damping effects are present at the edge and extend up to 300 eV beyond the edge. These damping effects are caused by the use of the EXAFS optic and intensify with increasing edge jump. They can result in a reduced absorption edge jump and a lower amplitude in the Fourier transformation (FT) of the EXAFS spectra, causing, among others, distortions in coordination numbers and bond distances. In the SI a direct comparison of LFP measured with both spectrometers is shown in Fig. S27 highlighting the extent of the effect. These damping effects are currently under investigation, with ongoing efforts to minimize their impact on the spectrum. Further extreme cases of pronounced damping, along with the optimal sample thickness, are provided in the SI (see Fig. S28 and S29).

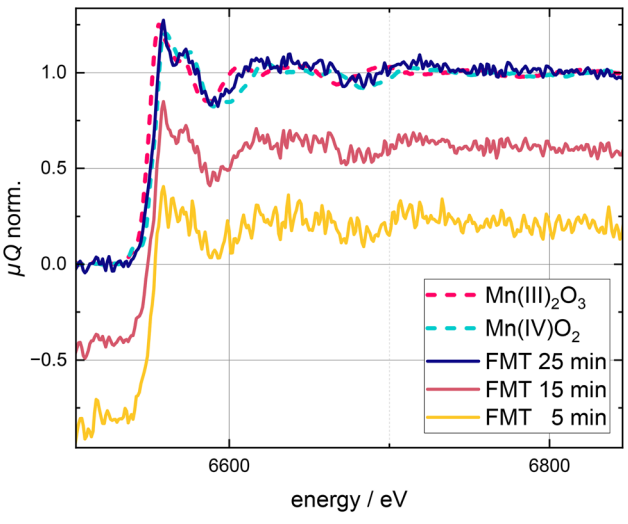

Fig. 3 Normalized XANES spectra of pristine FMT (prior charging) measured at the Mn K-edge for different measurement times in comparison with the references Mn_2O_3 and MnO_2 using the XANES optimized spectrometer. The lower SNR is mostly due to the sodium (Na) as anode material, instead of lithium compared to the LFP in Fig. 2.

Compared to XANES optimized measurements of LFP a broader spectral bandwidth could be measured at the same time, which is also shown by the unnormalized spectra (*cf.* Fig. S10 and S16 in the SI). The evolution of the spectral features for F6M4 is observed during charge, although the scale of change is substantially lower compared to the results of LFP (see Fig. 2). This was anticipated based on previous studies of other comparable layered O3-type materials. Additionally, while LFP cycles between Fe(II) and Fe(III), the layered materials are expected to cycle between Fe(III) and Fe(IV).

Fig. S21 (top, SI) shows the first and last spectra of the F6M4 sample during charging, compared to reference spectra of Fe_2O_3 (Fe(III)) and Fe_3O_4 (Fe(II,III)) measured on the same laboratory XAS setup, and $SrFeO_3$ (Fe(IV)), measured at beamline B18 of the Diamond Light Source (DLS) and published by Mahato *et al.* 2025.[61] The spectra have been aligned and normalized to allow for comparison of their absorption edge positions. The edge position of F6M4 lies between that of the Fe(III) and Fe(IV) references, indicating an average oxidation state of Fe in F6M4 that is higher than +III. This interpretation is further supported by the quantitative determination of the edge positions, obtained by interpolating the energy at which the normalized absorption crosses is 0.5: $E_0(Fe_2O_3) = 7124.90$ eV ± 0.03 eV, $E_0(SrFeO_3) = 7127.89$ eV ± 0.06 eV, and $E_0(F6M4) = 7125.79$ eV ± 0.03 eV.

While this supports the presence of Fe in an oxidation state between Fe(III) and Fe(IV), we emphasize that absorption edge position alone is not a definitive measure of oxidation state, as it can also be influenced by coordination environment and covalency.[56,62] Additionally, although reference compounds provide a useful guideline, the different chemical composition and structure of $SrFeO_3$ compared to the Fe–Mn oxide phase in F6M4 precludes its use in quantitative LCF analysis. For accurate LCF, reference standards should closely match the local

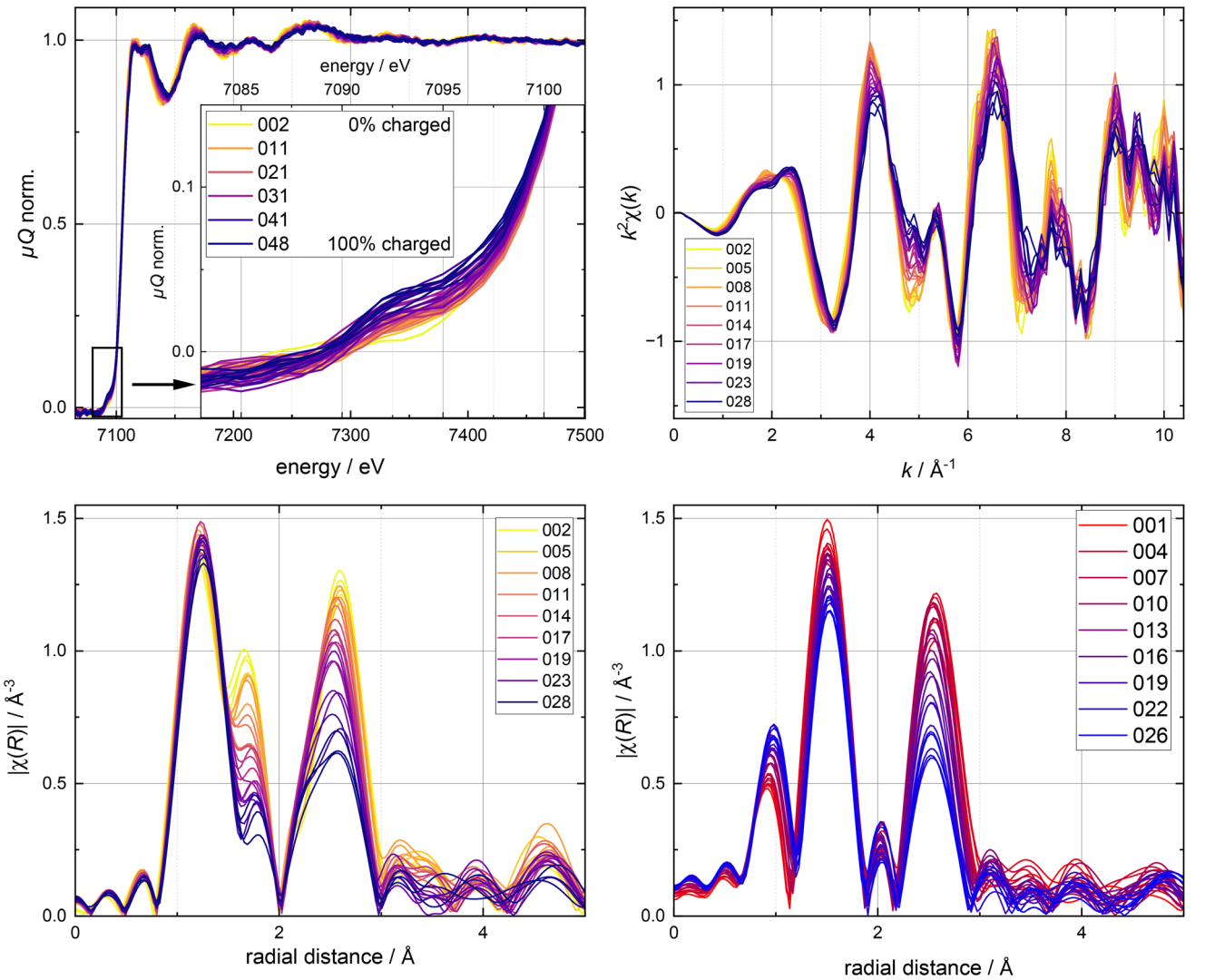

Fig. 4 (Top, left) Normalized *operando* EXAFS optimized measurement of F6M4 during charge at a C/20 rate (within the potential window of 1.5–4.3 V *vs.* Na^+/Na), with a measurement time of 15 min per spectrum (3 × binning). The inset highlights changes in the pre-edge. (Top, right) k^2-weighted EXAFS signal of F6M4, measured over 25 min using 5 × binning to improve SNR. (Bottom, left) FT of the EXAFS signal of F6M4. (Bottom, right) FT-EXAFS of FMM recorded with a measurement time of 25 min and 5 × binning (see Fig. S19, left in the SI for the corresponding k^2-weighted EXAFS signal). For both FT plots, the transformation was performed in a *k*-range of 3–11 $Å^{-1}$. The raw (unnormalized) data of F6M4 and FMM, including the discharge period, are shown in Fig. S16 and S17 in the SI.

chemical and structural environment present in the sample,[56,63] however, reference Fe(IV) oxides resembling the F6M4 and FMM materials are generally lacking. Furthermore, the $SrFeO_3$ spectrum was not collected on the same instrument as the sample data, introducing potential instrumental shifts and resolution differences. For these reasons, we include the comparison to Fe(IV) compounds as qualitative context only. Notably, the edge position of F6M4 remains effectively unchanged throughout the charging process (see Table S4, SI, for a summary of E_0 values of all measured references and first and last F6M4 states). While electrochemical data and the sample composition suggest a change in Fe oxidation state towards Fe(IV), this change is difficult to confirm solely based on the edge position, as no significant shift is observed.

As shown in the inset of Fig. 4 (top, left), a small pre-edge feature appears during charging, which may indicate distortions in the [FeO_6] octahedra by the cooperative Jahn–Teller effect (CJTE),[64] or Fe migration to tetrahedral sites.[65] When comparing the first and last spectrum of the charge and discharge cycle it is observed that this change is almost completely reversible, as shown in Fig. 5 (left). This reversibility of the species change is also supported by the measured capacity. During charge a total capacity of 141 mA h g^{-1} was reached, while during discharge a total capacity of 150 mA h g^{-1} was measured. The discharge capacity exceeding the charge capacity is expected as the pristine (as-synthesized) electrode materials contain less than one Na per formula unit, *i.e.*, less than one Na can be extracted during the first discharge, while

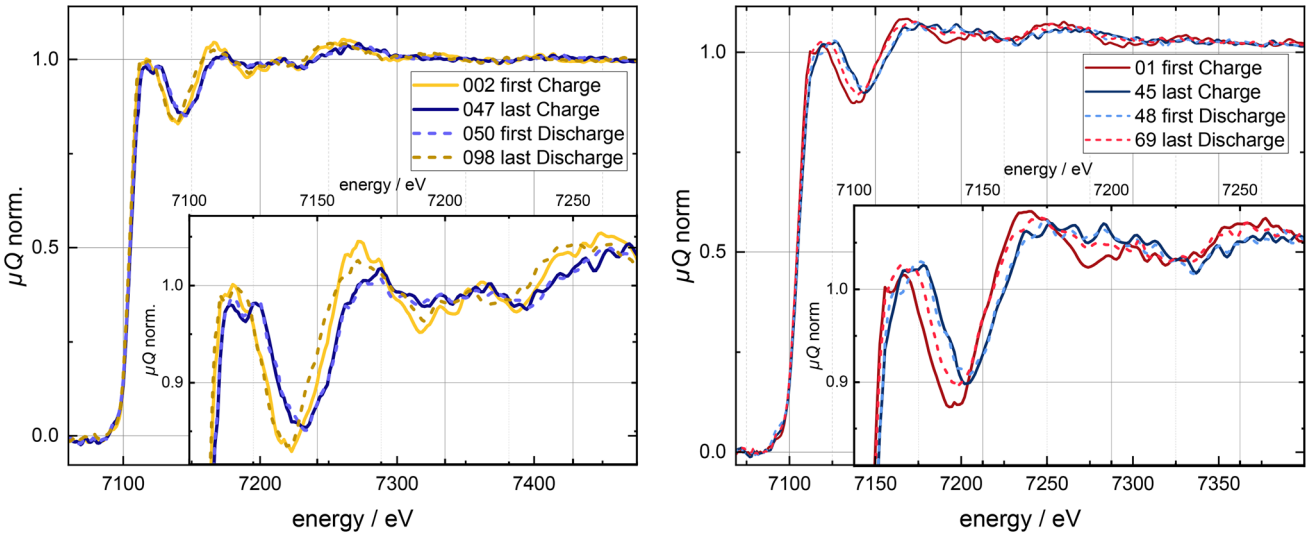

Fig. 5 First and last Fe K-edge spectrum, measured with the EXAFS optimized spectrometer, of charge and discharge of F6M4 (left) and FMM (right) with an enlargement of 150 eV beyond the edge in the insets. The data was 3× binned resulting in 15 min measurement time per spectrum. The raw spectra of the complete cycle for both materials, as well as the normalized spectra of FMM, are shown in the SI (see Fig. S16–S18).

insertion of up to one Na per formula unit is possible during charge.

The k^2-weighted EXAFS signal of F6M4 is shown in Fig. 4 (top, right) and was obtained from 5× binned (25 min measurement time) data to increase the SNR for higher k-values. In the k^2-weighted EXAFS of F6M4 the shifts and decrease/increase in intensity of the oscillation are more observable compared to the normalized spectra. The FT of the EXAFS signal in Fig. 4 (bottom, left) can provide information on the bond distance, disorder, and redox effects, among other factors.The dominant peaks in the FT-EXAFS of F6M4 are located at ∼1.2 Å, accompanied by a smaller peak at ∼1.6 Å, and ∼2.5 Å. Deviations between the peak positions in the FT-EXAFS and the actual bonding distances of 0.2–0.5 Å are expected due to the uncorrected phase shift that leads to lower apparent FT-EXAFS peak values.[66,67] Hence, the dominant peak at ∼1.2 Å and the smaller peak at ∼1.6 Å likely correspond to first shell Fe–O bonds, which are in the range of 1.7–2.3 Å.[68–70] The observation of two distinct peaks in the FT-EXAFS suggests the presence of multiple Fe–O bonding environments in the material, which likely arise from distortions of the [FeO_6] octahedra. These distortions may be attributed to a CJTE induced by the presence of Mn^{3+}.[71,72] While mild Fe–O bond splitting has previously been reported in the literature – for example, by Kwok *et al.* 2024 [71] and Behera *et al.* 2025 [73] (preprint) – the degree of splitting observed in our study is notably stronger. Similar or even more pronounced TM–O bond splittings have been observed in other systems, including Mn–O,[71,74] Co–O,[73] Ni–O,[75–77] and Cu–O.[74] While such behavior is not unprecedented, further verification of the observed Fe–O bond splitting is necessary. Complementary techniques such as temperature-dependent FT-EXAFS[75] (where the splitting is expected to diminish at elevated temperatures if driven by CJTE), Raman spectroscopy,[73] hard X-ray photoelectron spectroscopy (HAXPES),[73] pair distribution function (PDF) analysis *via* neutron scattering,[75,76] and Mössbauer spectroscopy[78] could provide additional insights to confirm the origin and nature of the distortion.

During charging, the peak intensity at ∼1.6 Å decreases significantly, accompanied by a broadening and the emergence of a shoulder in the second-shell peak at ∼2.5 Å. This behavior suggests a reduction in local structural distortion, potentially related to the diminishing Jahn–Teller effect as Mn^{3+} is oxidized.[79] Although the feature at 1.6 Å might partially result from overlapping contributions or superposition of multiple scattering paths, its distinct shift to higher R – contrary to the second-shell peak, which shifts to lower R – points to a real change in the local coordination environment. As shown in the SI (Fig. S25), the individual path contributions from the EXAFS fits (see discussion below) do not indicate any significant superposition at ∼1.6 Å within the applied model.

The reversible nature of these changes upon discharge (see Fig. S20 in the SI), coupled with the pre-existing peak splitting in the pristine state, supports a CJTE where correlated distortions across multiple Fe sites create long-range ordered structural modifications. The second dominant peak at ∼2.5 Å is assigned to an Fe–TM bond (Fe–Mn or Fe–Fe between 2.5–3.0 Å)[70,80] or to an Fe–Na bond (2.7–3.2 Å).[80]

For a quick analysis of the Fe–O bond distance, a quick first shell (QFS) path can be fitted using ARTEMIS from the Demeter software package.[55] It provides a structureless way of computing the scattering amplitude and phase shift of the first coordination shell well enough to offer a preliminary estimate of real bond distances.[81] The QFS function is only fitting one path using the EXAFS equation.[82,83] For an accurate fit and/or to include contributions from the second shell and beyond, several scattering paths need to be included, which are obtained from the complete atomic structure. This will be further discussed below. The QFS fit, shown in Fig. S25 (left) in the SI,

demonstrates that the model fails to properly reproduce the spectrum due to the splitting of the Fe–O bond. The fit attempts to compensate for this limitation by applying an nonphysically high amplitude reduction factor S_0^2 of 7.4 and high E_0 shift of −13,5 eV. As shown in Fig. S25 in the SI, the individual path contributions from the EXAFS fits do not indicate a superposition (see discussion above) of scattering paths at ∼1.6 Å within the current used model. Although the resulting bond distance of 1.89 ± 0.14 Å falls within literature reported values,[68–70] it cannot be considered reliable.

For a more accurate fit and/or for fitting the beyond the first shell several paths need to be included. These are obtained from the model of the complete atomic structure. When applying the structural model based on the layered oxide O3-$Na_xFe_{0.5}Mn_{0.5}O_2$ derived from XRD measurements, the second-shell contribution can be successfully fitted, as illustrated in Fig. S25 (right). However, due to the limitations of the model – which does not account for the CJTE – the split Fe–O bond still cannot be accurately fitted. Even attempts to include a second Fe–O path with different initial parameters failed to resolve this issue. A more accurate structural model that incorporates the CJTE, as done in the work by Nagle-Cocco *et al.* 2024,[75] is therefore required. In the O3-model EXAFS fit, only the Fe–Fe bond was modeled for the second peak. Due to the significant overlap between the Fe–Fe and Fe–Mn scattering paths, distinguishing between these contributions is not feasible. The fitting results are summarized in Table S5 in the SI, yielding a bond distance of 2.94 ± 0.06 Å for the Fe–TM (Fe/Mn) interaction and 3.21 ± 0.06 Å for the Fe–Na bond. These values are consistent with literature data[68,69,80] and preliminary Rietveld refinement of the XRD pattern.

During charge, the second peak is decreasing significantly, indicating disorder or oxidation/reduction effects in the materials. To better visualize the evolution of the peaks during charging, Gaussian profiles were applied to extract the absolute height and position of the two main features. The results are presented in Fig. S22 and S23 in the SI and confirm the strong decrease in intensity for the second dominant peak and show a small shift of the first peak and its adjacent smaller peak of approximately 0.06 Å and 0.01 Å respectively.

The second material investigated with Fe K-edge EXAFS optimized measurement was FMM (see Section 2.1.2). This sample, like F6M4, was compared to measured reference spectra of Fe_2O_3 (Fe(III)), Fe_3O_4 (Fe(II,III)), and $SrFeO_3$ (Fe(IV)), the latter obtained from Mahato *et al.* 2025.[61] Changes in the spectra during charge are observed for this material as well (see Fig. 5 (right) and Fig. S17–S19 in the SI). Upon closer examination of the white line (first peak beyond the edge), this feature exhibits a more pronounced shift towards higher energies or peak broadening compared to F6M4 (Fig. 5 (left)). This behavior is also evident from the edge position shift of nearly 1 eV between the first and last spectrum, as shown in Fig. S21 (bottom) and summarized in Table S4 in the SI. This could be attributed to a transition to a different species in FMM, possibly due to the doping of Mg, or by the fact, that the calculated specific capacity for this material of 224.6 mA h g^{-1} (close to 242.6 mA h g^{-1} for F6M4) was closer reached with a measured capacity of 183 mA h g^{-1} after reaching the potential limit of 4.3 V *vs.* Na^+/Na. The results in Fig. 5 (right) also show that the change of the Fe species in the cell does not completely reverse during discharge. The measured capacity for the discharge cycle is only 94 mA h g^{-1} which is only about 50% of the capacity reached during charge of the FMM and could be related to the incomplete reversal of the species. Additionally, we see signs of poor electrical contact through the battery 4.5 h after starting discharge (see SI Fig. S4, right). This could have increased the overpotential resulting in a faster discharge. However, this could also be due to irreversible structural rearrangements such as Fe migration or severe stacking faults as discussed in previous work.[64,84–87]

The FT-EXAFS signal of FMM (see Fig. 4, bottom right) also exhibits two dominant peaks around 1.49 Å and 2.52 Å. However, in contrast to F6M4, no peak splitting or signatures of cooperative Jahn–Teller distortions are observed in the pristine or charged states. This behavior may be attributed to the presence of Mg^{2+}, which stabilizes the lattice and shifts the oxidation state of Mn closer to +IV, thereby suppressing local Jahn–Teller distortions and promoting a more uniform Fe–O coordination.[88–90] A smaller peak at ∼2.0 Å in FMM can be attributed to a superposition of Fe–O and Fe–Fe/Na paths, as supported by the individual path contributions from the EXAFS fits shown in the SI (Fig. S26).

When comparing the FT-EXAFS of FMM and F6M4, it is evident that both exhibit a decrease in peak intensity during charging, with the second dominant peak in the FT-EXAFS of FMM decreasing by approximately 40%. Additionally, the first peak shifts toward higher radial distances by about 0.03 Å. A peak analysis similar to that performed for F6M4 was also carried out for FMM, with the results shown in Fig. S22 and S24 in the SI. The first peak is most likely associated with an Fe–O bond, but with a significantly longer bond length than observed in F6M4, likely due to the absence of the CJTE. The second peak can be attributed to Fe–TM and Fe–Na bonds, similar to F6M4. QFS fitting and full O3-model EXAFS fitting on the initial spectrum of FMM, as done for F6M4, support these interpretations. For FMM, both fitting approaches yielded good agreement, successfully reproducing the first and second coordination shells. This improved fit performance is most likely due to the absence of the CJTE in FMM.

The results, shown in Fig. S26 in the SI, yield bond distances of 1.96 ± 0.04 Å for the Fe–O bond from the QFS fit, and 1.95 ± 0.04 Å from the O3 model fit. Additionally, the O3-model EXAFS fit provides bond distances of 2.96 ± 0.03 Å for the Fe–TM bond and 3.16 ± 0.08 Å for the Fe–Na bond, which are in good agreement with values reported in the literature.[68–70,80] It should be noted that this represents a preliminary attempt at a full EXAFS fit, but it demonstrates that the O3 structure is an appropriate model for FMM. A more detailed fit, including additional scattering paths, would be required for improved accuracy but lies beyond the scope of this study.

When comparing the Fe K-edge XANES region of the spectra of F6M4 and FMM with those of FeO, Fe_2O_3, Fe_3O_4 and $SrFeO_3$ [61] no clear match is observed (see Fig. S21, SI) as mentioned already for F6M4. This lack of correlation likely results from

differences in both oxidation state distribution and local coordination environment between the binary iron oxide standards and the more complex iron–manganese oxide phases present in the samples. In contrast, the Mn K-edge XANES optimized measurements of FMT shows a clear resemblance to a known Mn-oxide reference, suggesting a simpler speciation for Mn in that case. These findings suggest that Fe in F6M4 and FMM is not present as a single, well-defined binary phase, but rather incorporated within a mixed Fe–Mn oxide framework and/or distributed over multiple species. This interpretation is further supported by XRD analysis of the pristine materials (see Fig. S6 and S7, SI), which confirms that Fe and Mn are incorporated into the same layered $NaTMO_2$ (O3-type) host structure. The XRD patterns show single-phase materials with minor unidentified impurities, indicating no separation into distinct Fe-only or Mn-only phases.

Operando EXAFS optimized measurements at the Fe K-edge were successfully performed during the cycling of F6M4 and FMM. The data acquired—within a measurement time of 15 to 25 minutes per spectrum—were of sufficient quality to yield valuable insights into the local structure and coordination environment of Fe within the cells. FT-EXAFS analysis provided qualitative information on the evolution of Fe coordination during cycling. For FMM, QFS fitting resulted in Fe–O bond distances that are consistent with values reported in the literature and those obtained from Rietveld refinement of XRD data. Furthermore, applying the O3-structural model enabled EXAFS fitting of the second shell, allowing the extraction of Fe–TM and Fe–Na bond distances and demonstrating the feasibility of detailed FT-EXAFS analysis when an accurate structural model is available.

In contrast, for F6M4, neither the QFS nor the O3-model EXAFS fits produced reliable Fe–O bond distances, likely due to the influence of the CJTE. Consequently, Fe–TM and Fe–Na bond distances obtained from the O3-model fit for F6M4 should be interpreted with caution, given the structural model's limitations. Structural models used for EXAFS fitting, such as the one in this work, can be derived from X-ray diffraction measurements (*e.g.*, *via* Crystallographic Information Files, CIF[91]). A comprehensive EXAFS fitting of all *operando* spectra was not conducted, as it would exceed the scope of this study.

4 Conclusions

Laboratory *operando* XANES and EXAFS measurements on battery materials with the DANOISE cell were successfully conducted on two different von Hámos spectrometers with HAPG optics. The Fe K-edge of LFP and of two O3-type layered oxides for Na-ion batteries was measured during charge and discharge as a proof of principle. Mn K-edge measurements of O3-NaFMT were conducted as well. However, due to electrochemical malfunction, the *operando* experiment was not possible. With measurement times of 15 min per spectrum the SNR was sufficient enough to perform LCF on the LFP and FMT XANES optimized measurements used to investigate the ratios of Fe valence states in the materials and thus tracking the redox reaction for LFP or proving possible air poisoning of the FMT within the cell. Furthermore, EXAFS was acquired on F6M4 and FMM using 25 minutes of exposure time with an EXAFS optimized spectrometer. The FT-EXAFS showed changes in bonding distances, distortion effects and changes in coordination geometry. To obtain reliable quantitative results from this data, especially when performing EXAFS-fitting, longer measurement time are required, compared to only conducting a XANES experiment.

Since the usable photon flux of the spectrometer increases with higher energy, investigation of other 3d TM such as Co, Ni, Cu, *etc*. can be conducted with shorter measurement time per spectrum compared to the Fe K-edge, if the elemental concentration is the same. The current spectral limitation of the XANES optimized spectrometer is about 18 keV, which means that K-edges up to Zr (17998 eV)[38] and L-edges of the 5d-TM are measurable. One crucial part to measure with such short acquisition times was the use of an optimized micro focus X-ray tube, which already reached 30 W at 15 keV. Further development in novel X-rays sources, optics and detectors can increase the efficiency and measurable spectral bandwidth of these spectrometers even further.

Nevertheless, despite the high efficiency of these laboratory spectrometers, short cycle rate such as C/0.5 or C/1 as shown in Yan *et al.* 2021 [9] are not applicable for the *operando* investigation of Na-ion based materials with the elemental concentration in this work.

This work demonstrates the feasibility of conducting laboratory-based *operando* XAS measurements on batteries, providing insights into the evolution of the electronic structure under realistic operating conditions. In addition to synchrotron XAS and XRD measurements, these findings enable further development and optimization of battery materials through *in situ* and *operando* laboratory investigations. Synchrotron beam time for *operando* studies can be prepared and used more efficiently by focusing on measurements that cannot be performed in the laboratory, such as high-speed cycling or spatially resolved experiments. Additionally, in combination with crystallographic information (CIF) from XRD measurements, FT-EXAFS fitting can be performed. For amorphous battery materials,[92] laboratory XAS serves as a valuable alternative to XRD. These results highlight the potential of laboratory-based techniques, such as the von Hámos spectrometers in this work, to complement large-scale facilities and advance battery research.

Author contributions

Sebastian Praetz: conceptualization, investigation/formal analysis/validation (XAFS measurements, qualitative XAFS analyses), project administration, resources (reference material), software, visualization, writing – original draft, writing – review and editing. Morten Johansen: conceptualization, investigation/formal analysis/validation (sample selection, sample preparations), writing – original draft, writing – review and editing. Delf Kober: software (electrochemical cycling), resources (provision reference materials, instrumentation), writing – original draft, writing – review editing. Marko Tesic: methodology, software (XAFS measurements). Christopher

Schlesiger: supervision, validation (XAFS measurements, XAFS methodology and software), writing – review and editing. Dorthe Ravnsbæk: supervision, writing – review and editing. Birgit Kanngießer: supervision, funding acquisition, writing – review and editing.

Conflicts of interest

There are no conflicts to declare.

Data availability

The data supporting this article have been included as part of the SI. Furthermore, the raw data for this article – including the XANES, EXAFS and XRD measurements, the CIF used for the EXAFS fitting procedure and as well the galvanostatic potential profiles – are available on Zenodo at **https://doi.org/10.5281/zenodo.14922524**.

Supplementary information is available at **https://doi.org/10.1039/d5ja00155b**. This includes complete potential-time curves of the measured battery materials, as well as XRD patterns and Rietveld refinements of FMT, F6M4, FMM, and synthesized LFP in their pristine states. Additionally, it provides unnormalized XAFS data from both XANES- and EXAFS-optimized measurements, along with Fourier-transformed EXAFS analyses and linear combination fitting results. A comparison between data collected using the XANES- and EXAFS-optimized spectrometers highlights the differences in spectral quality and interpretation between the two setups.

Acknowledgements

MJ and DR thank the Novo Nordic Foundation (grant no. NNF20OC0062068), and the Danish National Research Foundation (grant no. DNRF189) through the Center for Sustainable Energy Materials (CENSEMAT). We also thank Daniel Grötzsch for his assistance with the 3D illustration. Furthermore, we thank Michael A. Hayward from the Department of Chemistry at University of Oxford for providing the data of the Fe K-edge measurement of $SrFeO_3$ (supported by the grant Energy Materials Block Allocation Group SP14239).

Notes and references

1 IEA, *Batteries and Secure Energy Transitions – Analysis*, International Energy Agency, 2024, available from: **https://www.iea.org/reports/batteries-and-secure-energy-transitions**.

2 M. Fichtner, K. Edström, E. Ayerbe, M. Berecibar, A. Bhowmik, I. E. Castelli, *et al.*, Rechargeable Batteries of the Future—The State of the Art from a BATTERY 2030+ Perspective, *Adv. Energy Mater.*, 2022, **12**(17), 2102904, DOI: **10.1002/aenm.202102904**.

3 B. E. Lebrouhi, S. Baghi, B. Lamrani, E. Schall and T. Kousksou, Critical materials for electrical energy storage: Li-ion batteries, *J. Energy Storage*, 2022, **55**, 105471, available from: **https://www.sciencedirect.com/science/article/pii/S2352152X22014633**.

4 M. Patel, K. Mishra, R. Banerjee, J. Chaudhari, D. K. Kanchan and D. Kumar, Fundamentals, recent developments and prospects of lithium and non-lithium electrochemical rechargeable battery systems, *J. Energy Chem.*, 2023, **81**, 221–259, available from: **https://www.sciencedirect.com/science/article/pii/S2095495623001158**.

5 Improving the fundamental understanding of batteries via operando measurements, *Nat. Commun.*, 2022, **13**(1), 4723, available from: DOI: **10.1038/s41467-022-32245-9**.

6 S. M. Bak, Z. Shadike, R. Lin, X. Yu and X. Q. Yang, In situ/operando synchrotron-based X-ray techniques for lithium-ion battery research, *NPG Asia Mater.*, 2018, **10**(7), 563–580. Publisher: Nature Publishing Group, available from: **https://www.nature.com/articles/s41427-018-0056-z**.

7 A. P. Black, A. Sorrentino, F. Fauth, I. Yousef, L. Simonelli, C. Frontera, *et al.*, Synchrotron radiation based operando characterization of battery materials, *Chem. Sci.*, 2023, **14**, 1641–1665, DOI: **10.1039/D2SC04397A**.

8 P. Ghigna and E. Quartarone, Operando x-ray absorption spectroscopy on battery materials: a review of recent developments, *J. Phys.: Energy*, 2021, **3**(3), 032006, DOI: **10.1088/2515-7655/abf2db**.

9 T. Yan, C. Cheng and L. Zhang, Exploration of materials electrochemistry in rechargeable batteries using advanced in situ/operando x-ray absorption spectroscopy, *Electron. Struct.*, 2021, **3**(1), 013001, DOI: **10.1088/2516-1075/abea09**.

10 M. Balasubramanian, X. Sun, X. Q. Yang and J. McBreen, In situ X-ray diffraction and X-ray absorption studies of high-rate lithium-ion batteries, *J. Power Sources*, 2001, **92**(1), 1–8, available from: **https://www.sciencedirect.com/science/article/pii/S0378775300004936**.

11 A. Deb, U. Bergmann, E. J. Cairns and S. P. Cramer, X-ray absorption spectroscopy study of the Li_xFePO_4 cathode during cycling using a novel electrochemical *in situ* reaction cell, *J. Synchrotron Radiat.*, 2004, **11**(6), 497–504, DOI: **10.1107/S0909049504024641**.

12 M. Wagemaker, D. Lützenkirchen-Hecht, A. A. van Well and R. Frahm, Atomic and Electronic Bulk versus Surface Structure: Lithium Intercalation in Anatase TiO_2, *J. Phys. Chem. B*, 2004, **108**(33), 12456–12464, DOI: **10.1021/jp048567f**.

13 W. Malzer, C. Schlesiger and B. Kanngießer, A century of laboratory X-ray absorption spectroscopy – A review and an optimistic outlook, *Spectrochim. Acta, Part B*, 2021, **177**, 106101, DOI: **10.1016/j.sab.2021.106101**.

14 P. Zimmermann, S. Peredkov, P. M. Abdala, S. DeBeer, M. Tromp, C. Müller, *et al.*, Modern X-ray spectroscopy: XAS and XES in the laboratory, *Coord. Chem. Rev.*, 2020, **423**, 213466, DOI: **10.1016/j.ccr.2020.213466**.

15 G. T. Seidler, D. R. Mortensen, A. J. Remesnik, J. I. Pacold, N. A. Ball, N. Barry, *et al.*, A laboratory-based hard x-ray monochromator for high-resolution x-ray emission spectroscopy and x-ray absorption near edge structure measurements, *Rev. Sci. Instrum.*, 2014, **85**, 113906, DOI: **10.1063/1.4901599**.

16 C. Schlesiger, L. Anklamm, H. Stiel, W. Malzer and B. Kanngießer, XAFS spectroscopy by an X-ray tube based spectrometer using a novel type of HOPG mosaic crystal and optimized image processing, *J. Anal. At. Spectrom.*, 2015, **30**, 1080–1085, DOI: 10.1039/C4JA00303A.

17 Z. Németh, J. Szlachetko, É. G. Bajnóczi and G. Vankó, Laboratory von Hámos X-ray spectroscopy for routine sample characterization, *Rev. Sci. Instrum.*, 2016, **87**, 103105, DOI: 10.1063/1.4964098.

18 A. P. Honkanen, S. Ollikkala, T. Ahopelto, A. J. Kallio, M. Blomberg and S. Huotari, Johann-type laboratory-scale x-ray absorption spectrometer with versatile detection modes, *Rev. Sci. Instrum.*, 2019, **90**, 033107, DOI: 10.1063/1.5084049.

19 H. V. Le, S. Parishan, A. Sagaltchik, C. Göbel, C. Schlesiger, W. Malzer, *et al.*, Solid-State Ion-Exchanged Cu/Mordenite Catalysts for the Direct Conversion of Methane to Methanol, *ACS Catal.*, 2017, **2**(7), 1403–1412, DOI: 10.1021/acscatal.6b02372.

20 M. Dimitrakopoulou, X. Huang, J. Kröhnert, D. Teschner, S. Praetz, C. Schlesiger, *et al.*, Insights into Structure and Dynamics of (Mn,Fe)O_x-Promoted Rh Nanoparticles, *Faraday Discuss.*, 2018, **208**, 207–225, DOI: 10.1039/c7fd00215g.

21 R. L. Oliveira, M. C. B. Ghorbel, S. Praetz, D. Meiling, C. Schlesiger, R. Schomäcker, *et al.*, Confinement of Cobalt Species in Mesoporous N-Doped Carbons and the Impact on Nitroarene Hydrogenation, *ACS Sustainable Chem. Eng.*, 2020, **8**, 11171–11182, DOI: 10.1021/acssuschemeng.0c02365.

22 M. F. Bekheet, P. D. K. Nezhad, N. Bonmassar, L. Schlicker, A. Gili, S. Praetz, *et al.*, Steering the Methane Dry Reforming Reactivity of Ni/La_2O_3 Catalysts by Controlled *in situ* Decomposition of Doped La_2NiO_4 Precursor Structures, *ACS Catal.*, 2021, **11**, 43–59, DOI: 10.1021/acscatal.0c04290.

23 R. L. Oliveira, K. A. Ledwa, O. Chernyayeva, S. Praetz, C. Schlesiger and L. Kepinski, Cerium Oxide Nanoparticles Confined in Doped Mesoporous Carbons: A Strategy to Produce Catalysts for Imine Synthesis, *Inorg. Chem.*, 2023, **62**, 13554–13565, DOI: 10.1021/acs.inorgchem.3c01985.

24 F. Ebert, P. Ingale, S. Vogl, S. Praetz, C. Schlesiger, N. Pfister, *et al.*, Cobalt(II) Nanoclusters Incorporated in Ordered Mesoporous Al2O3 for Stable and Coke-Resistant Propane Dehydrogenation, *ACS Catal.*, 2024, (14), 9993–10008, DOI: 10.1021/acscatal.4c02067.

25 A. Gili, M. F. Bekheet, F. Thimm, B. Bischoff, M. Geske, M. Konrad, *et al.*, One-pot synthesis of iron-doped ceria catalysts for tandem carbon dioxide hydrogenation, *Catal.:Sci. Technol.*, 2024, **6**, 4174–4186, DOI: 10.1039/d4cy00439f.

26 X. Zhao, P. Pachfule, S. Li, T. Langenhahn, M. Ye, C. Schlesiger, *et al.*, Macro/Microporous Covalent Organic Frameworks for Efficient Electrocatalysis, *J. Am. Chem. Soc.*, 2019, **141**, 6623–6630, DOI: 10.1021/jacs.9b01226.

27 P. W. Menezes, C. Walter, J. N. Hausmann, R. Beltrán-Suito, C. Schlesiger, S. Praetz, *et al.*, Boosting Water Oxidation through In Situ Electroconversion of Manganese Gallide: An Intermetallic Precursor Approach, *Angew. Chem., Int. Ed.*, 2019, **58**, 16569–16574, DOI: 10.1002/anie.201909904.

28 J. Wang, A. Gili, M. Grünbacher, S. Praetz, J. D. Epping, O. Görke, *et al.*, Silicon oxycarbonitride ceramic containing nickel nanoparticles: From design to catalytic application, *Mater. Adv.*, 2021, **2**, 1715–1730, DOI: 10.1039/d0ma00917b.

29 H. Yang, X. Wang, S. Praetz, S. Pang, O. Görke, M. F. Bekheet, *et al.*, Photolithographic additive manufacturing of high-entropy perovskite oxides from synthesized multimetallic polymeric precursors, *J. Eur. Ceram. Soc.*, 2025, **45**, 116812, DOI: 10.1016/j.jeurceramsoc.2024.116812.

30 D. Motz, S. Praetz, C. Schlesiger, J. Henniges, F. Böttcher, B. Hesse, *et al.*, Examining iron complexes with organic ligands by laboratory XAFS, *J. Anal. At. Spectrom.*, 2023, **38**, 391–402, DOI: 10.1039/D2JA00351A.

31 L. J. Bauer, F. Wieder, V. Truong, F. Förste, Y. Wagener, A. Jonas, *et al.*, Absorption Correction for 3D Elemental Distributions of Dental Composite Materials Using Laboratory Confocal Micro-X-ray Fluorescence Spectroscopy, *Anal. Chem.*, 2024, **96**(21), 8441–8449, DOI: 10.1021/acs.analchem.4c00116.

32 A. J. Kallio, A. Weiß, R. Bes, M. J. Heikkilä, M. Ritala, M. Kemell, *et al.*, Laboratory-scale X-ray absorption spectroscopy of 3d transition metals in inorganic thin films, *Dalton Trans.*, 2022, **51**, 18593–18602, DOI: 10.1039/d2dt02264h.

33 N. S. Genz, A. J. Kallio, R. Oord, F. Krumeich, A. Pokle, Ø. Prytz, *et al.*, Operando Laboratory-Based Multi-Edge X-Ray Absorption Near-Edge Spectroscopy of Solid Catalysts, *Angew. Chem., Int. Ed.*, 2022, **61**, e202209334, DOI: 10.1002/anie.202209334.

34 M. Johansen, J. K. Verdelin, A. J. Kallio, T. O. Kessler, S. Huotari and D. B. Ravnsbæk, DANOISE; a 3D Printable Battery Cell for Laboratory Operando X-Ray Diffraction and Absorption Spectroscopy, *Batteries Supercaps*, 2024, **8**, e202400033, DOI: 10.1002/batt.202400033.

35 S. Praetz, D. Grötzsch, C. Schlesiger, D. Motz, M. Würth, R. Zimmermann, *et al.*, In situ heating cell for temperature dependent transmission x-ray absorption spectroscopy (XAS) measurement with a laboratory based spectrometer, *Rev. Sci. Instrum.*, 2025, **96**(3), 035120, DOI: 10.1063/5.0253653.

36 O. J. Borkiewicz, K. M. Wiaderek, P. J. Chupas and K. W. Chapman, Best Practices for Operando Battery Experiments: Influences of X-ray Experiment Design on Observed Electrochemical Reactivity, *J. Phys. Chem. Lett.*, 2015, **6**(11), 2081–2085, DOI: 10.1021/acs.jpclett.5b00891.

37 B. L. Henke, E. M. Gullikson and J. C. Davis, X-Ray Interactions: Photoabsorption, Scattering, Transmission, and Reflection at E = 50-30,000 eV, Z = 1-92, *At. Data Nucl. Data Tables*, 1993, **54**(2), 181–342, available from: https://www.sciencedirect.com/science/article/pii/S0092640X83710132.

38 W. T. Elam, B. D. Ravel and J. R. Sieber, A new atomic database for X-ray spectroscopic calculations, *Radiat. Phys. Chem.*, 2002, **63**(2), 121–128, available from: https://

www.sciencedirect.com/science/article/pii/S0969806X01002274.

39 T. Zhao, H. Mahandra, R. Marthi, X. Ji, W. Zhao, S. Chae, *et al.*, An overview on the life cycle of lithium iron phosphate: synthesis, modification, application, and recycling, *Chem. Eng. J.*, 2024, **485**, 149923, available from: https://www.sciencedirect.com/science/article/pii/S1385894724014086.

40 P. Phogat, S. Dey and M. Wan, Comprehensive review of Sodium-Ion Batteries: Principles, Materials, Performance, Challenges, and future Perspectives, *Mater. Sci. Eng., B*, 2025, **312**, 117870, available from: https://www.sciencedirect.com/science/article/pii/S0921510724006998.

41 O. J. Borkiewicz, B. Shyam, K. M. Wiaderek, C. Kurtz, P. J. Chupas and K. W. Chapman, The AMPIX electrochemical cell: A versatile apparatus for in situ X-ray scattering and spectroscopic measurements, *J. Appl. Crystallogr.*, 2012, **45**, 1261–1269, DOI: 10.1107/S0021889812042720.

42 J. Lunt, Large-scale production, properties and commercial applications of polylactic acid polymers, *Polym. Degrad. Stab.*, 1998, **59**(1), 145–152. Biodegradable Polymers and Macromolecules, available from: https://www.sciencedirect.com/science/article/pii/S0141391097001481.

43 L. de Souza Vieira, A review on the use of glassy carbon in advanced technological applications, *Carbon*, 2022, **186**, 282–302, available from: https://www.sciencedirect.com/science/article/pii/S0008622321009982.

44 K. Klementiev and R. Chernikov, XAFSmass: a program for calculating the optimal mass of XAFS samples, *J. Phys.: Conf. Ser.*, 2016, **712**(1), 012008, DOI: 10.1088/1742-6596/712/1/012008.

45 C. Schlesiger, S. Praetz, R. Gnewkow, W. Malzer and B. Kanngießer, Recent progress in the performance of HAPG based laboratory EXAFS and XANES spectrometers, *J. Anal. At. Spectrom.*, 2020, **35**, 2298–2304, DOI: 10.1039/D0JA00208A.

46 W. Malzer, D. Grötzsch, R. Gnewkow, C. Schlesiger, F. Kowalewski, B. Van Kuiken, *et al.*, A laboratory spectrometer for high throughput X-ray emission spectroscopy in catalysis research, *Rev. Sci. Instrum.*, 2018, **89**(11), 113111, DOI: 10.1063/1.5035171.

47 J. Chen and M. S. Whittingham, Hydrothermal synthesis of lithium iron phosphate, *Electrochem. Commun.*, 2006, **8**(5), 855–858, available from: https://www.sciencedirect.com/science/article/pii/S1388248106001020.

48 M. H. Lee, T. H. Kim, Y. S. Kim and H. K. Song, Precipitation Revisited: Shape Control of LiFePO4 Nanoparticles by Combinatorial Precipitation, *J. Phys. Chem. C*, 2011, **115**(25), 12255–12259, DOI: 10.1021/jp201476z.

49 H. M. Rietveld, A profile refinement method for nuclear and magnetic structures, *J. Appl. Crystallogr.*, 1969, **2**(2), 65–71, DOI: 10.1107/S0021889869006558.

50 A. A. Coelho, TOPAS and TOPAS-Academic: an optimization program integrating computer algebra and crystallographic objects written in C++, *J. Appl. Crystallogr.*, 2018, **51**(1), 210–218, DOI: 10.1107/S1600576718000183.

51 Sigma-Aldrich, Nickel(II)-oxid; n.d. Quality grade 200, powder form, composition: Fe 24%, CAS-No: 31096-47-6. Catalog No. 436038, accessed January 2025, available from: https://www.sigmaaldrich.com/DE/de/product/aldrich/436038.

52 Sigma-Aldrich, iron(II) oxide (FeO);. Particle, -10 mesh, 99.9% trace metals basis, Catalog No. 400866, accessed February 2025, available from: https://www.sigmaaldrich.com/DE/de/product/aldrich/400866.

53 Honeywell/Fluka, iron(III) oxide (Fe_2O_3);. Powder, < 5 μm, ≥99%, Catalog No. 310050, accessed January 2025, available from: https://lab.honeywell.com/shop/iron-iii-oxide-310050.

54 Sigma-Aldrich. iron(II,III) oxide (Fe_3O_4);. Powder, < 5μ m, ≥95%, Catalog No. 310069, accessed January 2025, available from: https://www.sigmaaldrich.com/DE/de/product/aldrich/310069.

55 B. Ravel and M. Newville, ATHENA, ARTEMIS, HEPHAESTUS: data analysis for X-ray absorption spectroscopy using IFEFFIT, *J. Synchrotron Radiat.*, 2005, **12**, 537–541, DOI: 10.1107/S0909049505012719.

56 S. D. Kelly, D. Hesterberg and B. Ravel, in *Analysis of Soils and Minerals Using X-Ray Absorption Spectroscopy*, John Wiley and Sons, Ltd, 2008, pp. 387–463, DOI: 10.2136/sssabookser5.5.c14.

57 G. Ouvrard, M. Zerrouki, P. Soudan, B. Lestriez, C. Masquelier, M. Morcrette, *et al.*, Heterogeneous behaviour of the lithium battery composite electrode LiFePO4, *J. Power Sources*, 2013, **229**, 16–21, available from: https://www.sciencedirect.com/science/article/pii/S0378775312017314.

58 T. Ressler, J. Wong, J. Roos and I. L. Smith, Quantitative speciation of Mn-bearing particulates emitted from autos burning (methylcyclopentadienyl)manganese tricarbonyl-added gasolines using XANES spectroscopy, *Environ. Sci. Technol.*, 2000, **34**(6), 950–958, available from: https://hdl.handle.net/11858/00-001M-0000-0011-1B6A-D.

59 A. Manceau, M. A. Marcus and T. Lenoir, Estimating the number of pure chemical components in a mixture by X-ray absorption spectroscopy, *J. Synchrotron Radiat.*, 2014, **21**(5), 1140–1147, DOI: 10.1107/S1600577514013526.

60 A. Pattammattel, R. Tappero, D. Gavrilov, H. Zhang, P. Aronstein, H. J. Forman, *et al.*, Multimodal X-ray nano-spectromicroscopy analysis of chemically heterogeneous systems, *Metallomics*, 2022, **14**(10), mfac078, DOI: 10.1093/mtomcs/mfac078.

61 S. Mahato, X. Martínez de Irujo Labalde, H. Grievson, J. M. Mortimer, S. G. Booth, A. Menon, *et al.*, The Role of Fe(IV)-O Anion Redox Centers in the Electrochemical Behavior of Al- and Ga-Doped T-$LiFeO_2$, *Chem. Mater.*, 2025, **37**(9), 3171–3184, DOI: 10.1021/acs.chemmater.4c03322.

62 S. Calvin, *XAFS for Everyone*, CRC Press, Boca Raton, 1st edn, 2013.

63 S. Praetz, C. Schlesiger, D. A. Motz, S. Klimke, M. Jahns, C. Gottschalk, *et al.*, Can laboratory-based XAFS compete with XRD and Mössbauer spectroscopy as a tool for quantitative species analysis? Critical evaluation using the example of a natural iron ore, *PLoS One*, 2025, **20**(5), e0323678, DOI: **10.1371/journal.pone.0323678**.

64 B. Mortemard de Boisse, J. H. Cheng, D. Carlier, M. Guignard, C. J. Pan, S. Bordère, *et al.*, O3–$Na_xMn_{1/3}Fe_{2/3}O_2$ as a Positive Electrode Material for Na-Ion Batteries: Structural Evolutions and Redox Mechanisms upon Na^+ (De)intercalation, *J. Mater. Chem. A*, 2015, **3**, 10976–10989, DOI: **10.1039/C4TA06688J**.

65 Y. Li, Y. Gao, X. Wang, X. Shen, Q. Kong, R. Yu, *et al.*, Iron Migration and Oxygen Oxidation During Sodium Extraction from $NaFeO_2$, *Nano Energy*, 2018, **47**, 519–526, available from: **https://www.sciencedirect.com/science/article/pii/S2211285518301368**.

66 E. A. Stern, D. E. Sayers and F. W. Lytle, Extended x-ray-absorption fine-structure technique. III. Determination of physical parameters, *Phys. Rev. B:Condens. Matter Mater. Phys.*, 1975, **11**, 4836–4846, DOI: **10.1103/PhysRevB.11.4836**.

67 G. Bunker, *Introduction to XAFS: A Practical Guide to X-Ray Absorption Fine Structure Spectroscopy*, Cambridge Univ. Press, Cambridge, 2010.

68 O. C. Gagné and F. C. Hawthorne, Bond-length distributions for ions bonded to oxygen: results for the transition metals and quantification of the factors underlying bond-length variation in inorganic solids, *IUCrJ*, 2020, **7**(4), 581–629, DOI: **10.1107/S2052252520005928**.

69 M. Sawada, R. Iwamoto, T. Kotani and H. Sakakibara, Bond-length distributions in ionically bonded materials with decomposition by coordination environment, *J. Appl. Crystallogr.*, 2022, **55**(5), 1359–1367, DOI: **10.1107/S1600576722006884**.

70 O. J. Marques and C. U. Segre, Structural modeling of high-entropy oxides battery anodes using x-ray absorption spectroscopy, *J. Appl. Phys.*, 2024, **135**(22), 225001, DOI: **10.1063/5.0206316**.

71 C. Y. Kwok, S. Mallick, C. J. Pollock, A. Gutierrez, M. Dixit, J. R. Croy, *et al.*, Redox Mechanisms and Migration Tendencies in Earth-Abundant $0.7Li_2MnO_3{\cdot}0.3LiFeO_2$ Cathodes: Coupling Spin-Resolved X-ray Absorption Near Edge and X-ray Absorption Fine Structure Spectroscopies, *Chem. Mater.*, 2024, **36**(1), 300–312, DOI: **10.1021/acs.chemmater.3c02111**.

72 Y. Zheng, H. Xie, J. Li, K. S. Hui, Z. Yu, H. Xu, *et al.*, Insights into the Jahn-Teller Effect in Layered Oxide Cathode Materials for Potassium-Ion Batteries, *Adv. Energy Mater.*, 2024, **14**(14), 2400461, DOI: **10.1002/aenm.202400461**.

73 S. S. Behera, I. Lallar, A. K. Yogi, V. R. R. Medicherla, P. Rajput, A. Sagdeo, *et al.*, Local symmetry breaking and orbital glass behaviour in $CoFe_2O_4$; 2025, available from: **https://arxiv.org/abs/2506.16857**.

74 E. Hastuti, A. Subhan, P. Amonpattaratkit, M. Zainuri, T. Triwikantoro and S. Suasmoro, Oxidation state, local structure distortion, and defect structure analysis of Cu doped α-MnO_2 correlated to conductivity and dielectric properties, *Heliyon*, 2022, **8**(11), e11459, available from: **https://www.sciencedirect.com/science/article/pii/S2405844022027475**.

75 L. A. V. Nagle-Cocco, A. R. Genreith-Schriever, J. M. A. Steele, C. Tacconis, J. D. Bocarsly, O. Mathon, *et al.*, Displacive Jahn–Teller Transition in $NaNiO_2$, *J. Am. Chem. Soc.*, 2024, **146**(43), 29560–29574, DOI: **10.1021/jacs.4c09922**.

76 A. R. Genreith-Schriever, A. Alexiu, G. S. Phillips, C. S. Coates, L. A. V. Nagle-Cocco, J. D. Bocarsly, *et al.*, Jahn–Teller Distortions and Phase Transitions in $LiNiO_2$: Insights from Ab Initio Molecular Dynamics and Variable-Temperature X-ray Diffraction, *Chem. Mater.*, 2024, **36**(5), 2289–2303, DOI: **10.1021/acs.chemmater.3c02413**.

77 A. Demourgues, L. Gautier, A. V. Chadwick and C. Delmas, EXAFS study of the Jahn-Teller distortion in layered nickel oxyhydroxide, *Nucl. Instrum. Methods Phys. Res., Sect. B*, 1997, **133**(1), 39–44. Proceedings of the 1st international conference on synchrotron radiation in materials science, available from: **https://www.sciencedirect.com/science/article/pii/S0168583X9700459X**.

78 M. Tanaka, T. Tokoro and Y. Aiyama, Jahn-Teller Effects on Mössbauer Spectra of ^{57}Fe in $FeCr_2O_4$ and FeV_2O_4, *J. Phys. Soc. Jpn.*, 1966, **21**(2), 262–267, DOI: **10.1143/JPSJ.21.262**.

79 S. Wang, X. Guo, K. Huang, A. Achari, J. Safaei, Y. Lei, *et al.*, Cooperative Jahn-Teller effect and engineered long-range strain in manganese oxide/graphene superlattice for aqueous zinc-ion batteries, *Nat. Commun.*, 2025, **16**(1), 5191, DOI: **10.1038/s41467-025-60558-y**.

80 X. Li, D. Wu, Y. N. Zhou, L. Liu, X. Q. Yang and G. Ceder, O3-type $Na(Mn_{0.25}Fe_{0.25}Co_{0.25}Ni_{0.25})O_2$: A quaternary layered cathode compound for rechargeable Na ion batteries, *Electrochem. Commun.*, 2014, **49**, 51–54, available from: **https://www.sciencedirect.com/science/article/pii/S1388248114003129**.

81 B. Ravel, Artemis Software Documentation, Version 0.9.26: Quick First Shell, 2016, Software documentation, Licensed under CC BY-SA 3.0, Accessed 17 March 2025, **https://bruceravel.github.io/demeter/documents/Artemis/extended/qfs.html**.

82 J. J. Rehr and R. C. Albers, Theoretical approaches to x-ray absorption fine structure, *Rev. Mod. Phys.*, 2000, **72**, 621–654, DOI: **10.1103/RevModPhys.72.621**.

83 S. I. Zabinsky, J. J. Rehr, A. Ankudinov, R. C. Albers and M. J. Eller, Multiple-scattering calculations of x-ray-absorption spectra, *Phys. Rev. B:Condens. Matter Mater. Phys.*, 1995, **52**, 2995–3009, DOI: **10.1103/PhysRevB.52.2995**.

84 E. Boivin, R. A. House, J. Marie and P. G. Bruce, Controlling Iron Versus Oxygen Redox in the Layered Cathode $Na_{0.67}Fe_{0.5}Mn_{0.5}O_2$: Mitigating Voltage and Capacity Fade by Mg Substitution, *Adv. Energy Mater.*, 2022, **12**, 2200702, DOI: **10.1002/aenm.202200702**.

85 B. Silván, E. Gonzalo, L. Djuandhi, N. Sharma, F. Fauth and D. Saurel, On the Dynamics of Transition Metal Migration and its Impact on the Performance of Layered Oxides for Sodium-Ion Batteries: $NaFeO_2$ as a Case Study, *J. Mater. Chem. A*, 2018, **6**, 15132–15146, DOI: **10.1039/C8TA04890C**.

86 M. Reynaud, J. Serrano-Sevillano and M. Casas-Cabanas, Imperfect Battery Materials: A Closer Look at the Role of Defects in Electrochemical Performance, *Chem. Mater.*, 2023, **35**, 3345–3363, DOI: **10.1021/acs.chemmater.2c03481**.

87 A. Østergaard Drejer, M. S. Hansen, M. Johansen, J. Dunker, R. Poppe, J. Hadermann, *et al.*, Charge–Discharge Mechanisms in O3-$Na_xFe_{0.5}Mn_{0.5}O_2$ Na-Ion Battery Electrodes – Unraveling the Structure of the X-Phase, *Chem. Mater.*, 2025, **37**(14), 5234–5248, DOI: **10.1021/acs.chemmater.5c00961**.

88 I. Moiseev, A. Golubnichiy, A. Pavlova, A. Burov, A. Boev, A. Komayko, *et al.*, The rivet effect: a new insight into improving structural stability in Mg-doped Ni-rich single-crystal layered oxide cathodes for Li-ion batteries, *J. Mater. Chem. A*, 2025, **13**(17), 12581–12597, DOI: **10.1039/D4TA08998G**.

89 A. Chakraborty, R. A. House and M. S. Islam, Suppressing O-type stacking and cation migration with Mg and Si doping in P2-type Fe–Mn layered oxides for sodium-ion cathodes, *J. Mater. Chem. A*, 2025, **13**, 17615–17621, DOI: **10.1039/D5TA00804B**.

90 C. Zhao, Z. Yao, Q. Wang, H. Li, J. Wang, M. Liu, *et al.*, Revealing High Na-Content P2-Type Layered Oxides as Advanced Sodium-Ion Cathodes, *J. Am. Chem. Soc.*, 2020, **142**(12), 5742–5750, DOI: **10.1021/jacs.9b13572**.

91 S. R. Hall, F. H. Allen and I. D. Brown, The crystallographic information file (CIF): a new standard archive file for crystallography, *Acta Crystallogr., Sect. A:Found. Crystallogr.*, 1991, **47**(6), 655–685, available from: **https://journals.iucr.org/paper?S010876739101067X**.

92 J. Ding, D. Ji, Y. Yue and M. M. Smedskjaer, Amorphous Materials for Lithium-Ion and Post-Lithium-Ion Batteries, *Small*, 2024, **20**(5), 2304270, DOI: **10.1002/smll.202304270**.